

Theoretical Analysis of Resonant Tunneling Enhanced Field Emission

Yang Zhou¹, Ragib Ahsan,² Hyun Uk Chae,² Rehan Kapadia,² and Peng Zhang^{1,*}

¹*Department of Electrical and Computer Engineering, Michigan State University, East Lansing, Michigan 48824, USA*

²*Ming Hsieh Department of Electrical and Computer Engineering, University of Southern California, Los Angeles, California 90089, USA*

(Received 14 February 2023; revised 4 May 2023; accepted 23 June 2023; published 19 July 2023)

In this paper, we develop an exact analytical quantum theory for field emission from surfaces with a nearby quantum well, by solving the one-dimensional time-independent Schrödinger equation. The quantum well, which may be introduced by ions, atoms, nanoparticles, etc., is simplified as a square potential well with depth H , width d , and distance to the surface L . The theory is used to analyze the effects of the quantum well (d , H , and L), the cathode properties (work function W and Fermi energy E_F), and dc field F . It is found that the quantum well can lead to resonant tunneling enhanced field emission up to several orders of magnitude larger than that from bare cathode surfaces. In the meantime, the electron-emission-energy spectrum is significantly narrowed. The strong enhancement region is bounded by the conditions $eFL + H \geq W + C$ and $eFL \leq W$, with e being the elementary charge (positive) and C a constant dependent on dc field F . It is also found that the linear shift of resonance peaks in the electron-emission-energy spectrum with dc field F follows $\varepsilon_p = \varepsilon_{p0} - eFL$, with ε_{p0} being approximately the eigenenergies for electrons confined in a square potential well without a dc field. The theory provides insights for the design of high-efficiency field emitters, which can produce a high current and highly collimated electron beams.

DOI: 10.1103/PhysRevApplied.20.014043

I. INTRODUCTION

Field emission from solid surfaces is critical for many applications, such as flat-panel displays [1–3], electron microscopes [4–6], vacuum microelectronics [7,8], emerging vacuum nanoelectronic devices [9–13], x-ray sources [14,15], particle accelerators [16–18], and high-power microwave sources and amplifiers [19–26]. The presence of nanostructures or adsorbates (ions, atoms, molecules, etc.) on cathodes forms a nearby potential well(s) and modifies the surface-potential barrier, which has significant effects on the field-emission current and the corresponding emission-energy distribution [27–35]. The quantum well(s) can lead to resonant tunneling field emission, which deviates from Fowler-Nordheim characteristics [27–29]. Resonant effects in tunneling in field emission reported by Binh *et al.* [33,34] generated considerable interest to understand resonance contributions both experimentally [36–38] and theoretically [27,39–41]. The resonant tunneling through adsorbed atoms and molecules can produce highly enhanced localized field emission with a narrow energy spread, compared to clean surface regions [30]. In addition to resonant processes, nonresonant processes due to thinning of the surface barrier by positive ions have the potential to further enhance field emission [31,32].

Ion-enhanced field emission plays an important role in the deviation of breakdown voltage from the Paschen's law in a microscale gap (~ 1 – 10 μm) [31,42–47]. Another important characteristic of resonant tunneling is multiple resonant peaks in the field-emission energy spectrum. It is observed that resonance peaks shift linearly with dc voltage for sharp metallic nanotips ending with a single atom [33,34]. Therefore, it is worthwhile developing a generic model to systematically study those observations.

Early theoretical interpretation of field emission from metal surfaces with nearby adsorbates, nanoparticles, etc. uses Fowler-Nordheim-type equations, with an electric field or work function modified due to adsorbates [46,48]. By introducing a potential well outside the metal surface, the Schrödinger equation gives a more realistic description of the quantum tunneling process [31,32,49,50]. Wentzel-Kramers-Brillouin (WKB) methods are used to obtain an emission current from silicon emitters with an oxide layer [51,52], which may not reveal the resonance effects inside the quantum well [53]. A steady-state-balance transport equation based on the WKB approach for nanoparticles on top of a dielectric material on metallic cathodes reveals the experimentally observed steplike behavior in the current-voltage relationship [41]. Theoretical methods typically involve solving a stationary Schrödinger equation with boundary conditions of the wave function and its

*pz@egr.msu.edu

derivative continuity [27,39–41]. In particular, the Airy-function transfer-matrix method is broadly used for resonant tunneling diodes and multilayer-structure cathodes [40,54,55]. Density-functional theory is applied to analyze the field emission from atomically sharp tips, including the effects of electric fields and currents [56], which can be computationally expensive. It is desirable to use a simple generic exact quantum model for field emission with a nearby quantum well to study the effects of the well properties on field emission.

Here, we develop an analytical quantum theory for field emission from surfaces with a nearby quantum well, by exactly solving the one-dimensional (1D) time-independent Schrödinger equation. The theory includes the effects of the quantum well, i.e., well depth, well width, and distance from the well to metal surfaces. It predicts the conditions of the quantum well under which the field emission can be resonantly enhanced by several times to several orders of magnitude compared to field emission from bare cathode surfaces. This study provides insights for the design of a highly efficient field emitter to produce high current and highly collimated electron beams.

II. THEORETICAL FORMULATION

The 1D model considers electrons inside the metal ($x < 0$) with an initial longitudinal energy ε emitted to vacuum under an externally applied dc electric field F , as shown in Fig. 1. A quantum well is formed near the metal surface due to ions, atoms, nanoparticles, etc. with well depth H , well width d , and distance from left edge of the well to metal surface L . The potential profile reads

$$V(x) = \begin{cases} 0, & x < 0, \\ V_0 - eFx, & 0 \leq x < L, \\ V_0 - eFL - H, & L \leq x < L + d, \\ V_0 + eFd - eFx, & x \geq L + d, \end{cases} \quad (1)$$

where $V_0 = W + E_F$, with W and E_F being the work function and Fermi energy of the metal, respectively; e (>0) is the elementary charge. For simplicity, the effect of the image charge potential is ignored, and we assume that the region between the surface and the quantum well ($0 < x < L$) is a dielectric (with a relative permittivity of 1, i.e., vacuum) and the fields in this region ($0 < x < L$) and in the vacuum ($x > d + L$) are constant as F , and the top and bottom of the well are flat without considering distortion by the dc field F . The latter assumption is expected to be a better approximation if the quantum well has a larger aspect ratio, H/d ; a higher permittivity; or a smaller electric field.

To obtain the electron-transmission probability, we solve the 1D time-independent Schrödinger equation:

$$-\frac{\hbar^2}{2m} \frac{\partial^2 \psi(x)}{\partial x^2} + V(x)\psi(x) = \varepsilon\psi(x), \quad (2)$$

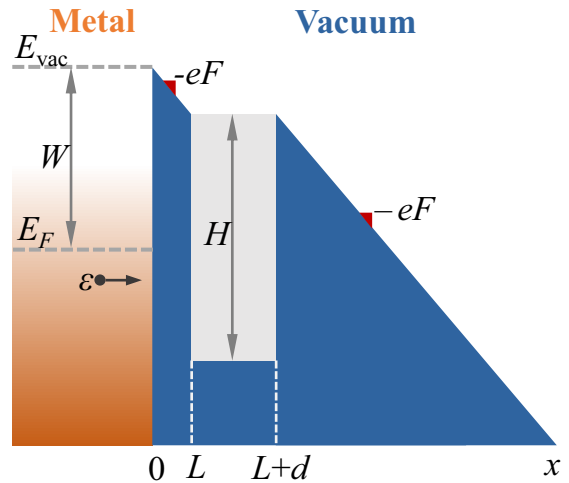


FIG. 1. Energy diagram of field electron emission through a triangular barrier deformed by a quantum well under externally applied dc field F . Incident electron has an initial longitudinal energy of ε . Metal has Fermi energy E_F and work function W . Quantum well has depth H , width d , and distance from the left edge of the quantum well to the metal surface L .

where \hbar is the reduced Planck constant, m is the electron rest mass (in all regions), $\psi(x)$ is the electron wave function, $V(x)$ is the potential given in Eq. (1), and ε is the initial longitudinal energy of electrons incident on the metal surfaces. For $x < 0$ (inside the metal), the exact solution of Eq. (2) is

$$\psi_I(x) = e^{ik_0x} + R e^{-ik_0x}, \quad x < 0, \quad (3)$$

with $k_0 = \sqrt{2m\varepsilon/\hbar^2}$ being the electron wave number and R the reflection coefficient. Equation (2) is the superposition of an incident plane wave and a reflected plane wave.

For $0 \leq x < L$, the solution can be obtained by transforming Eq. (2) into the form of $d^2\psi_{II}/d\eta_1^2 + \eta_1\psi_{II} = 0$, with $\eta_1 = (2meF/\hbar^2)^{1/3}[x + (\varepsilon - V_0)/eF]$, to yield

$$\psi_{II}(x) = aAi(-\eta_1) + bBi(-\eta_1), \quad (4)$$

which is a linear superposition of the Airy functions of the first and second kinds.

For $L \leq x < L + d$, the exact solution to Eq. (2) is

$$\psi_{III}(x) = p e^{ikx} + q e^{-ikx}, \quad (5)$$

where $k = \sqrt{2m[\varepsilon - (V_0 - H - eFL)]/\hbar^2}$ is the electron wave number inside the quantum well for an electron with an initial energy of ε .

For $x \geq L + d$, Eq. (2) is transformed into $d^2\psi_{IV}/d\eta_2^2 + \eta_2\psi_{IV} = 0$ with $\eta_2 = (2meF/\hbar^2)^{1/3}[x + (\varepsilon - (V_0 + eFd))/$

$eF]$ and the solution is

$$\psi_{IV} = T_t[Ai(-\eta_2) - Bi(-\eta_2)], \quad (6)$$

where T_t is the transmission coefficient. Equation (6) represents an outgoing traveling wave into the vacuum.

The imposition of the boundary conditions that ψ and $d\psi/dx$ are continuous at $x = 0$, $x = L$, and $x = L + d$ yields

$$\begin{aligned} 1 + R &= aA_1 + bB_1, \\ 1 - R &= \zeta(aA'_1 + bB'_1), \\ aA_2 + bB_2 &= pC_1 + qC_2, \\ \gamma(aA'_2 + bB'_2) &= pC_1 - qC_2, \\ pC_3 + qC_4 &= T_t(A_3 - iB_3), \\ pC_3 - qC_4 &= \gamma T_t(A'_3 - iB'_3), \end{aligned} \quad (7)$$

where $A_1 = Ai(-\eta_1(x = 0))$, $B_1 = Bi(-\eta_1(x = 0))$, $A'_1 = Ai'(-\eta_1(x = 0))$, $B'_1 = Bi'(-\eta_1(x = 0))$, $A_2 = Ai(-\eta_1(x = L))$, $B_2 = Bi(-\eta_1(x = L))$, $A'_2 = Ai'(-\eta_1(x = L))$, $B'_2 = Bi'(-\eta_1(x = L))$, $A_3 = Ai(-\eta_2(x = L + d))$, $B_3 = Bi(-\eta_2(x = L + d))$, $A'_3 = Ai'(-\eta_2(x = L + d))$, $B'_3 = Bi'(-\eta_2(x = L + d))$, $C_1 = e^{ikL}$, $C_2 = e^{-ikL}$, $C_3 = e^{ik(L+d)}$, $C_4 = e^{-ik(L+d)}$, $\zeta = i/k_0(2meF/\hbar^2)^{1/3}$, and $\gamma = i/k(2meF/\hbar^2)^{1/3}$. Ai' and Bi' are the first derivatives of Ai and Bi , respectively, with respect to their arguments. The transmission coefficient T_t is then obtained as

$$T_t = \frac{2}{\pi[P_2(A_1 + \zeta A'_1) + P_1(B_1 + \zeta B'_1)]}, \quad (8)$$

where $P_1 = A_2/\gamma(K_1C_1 - K_2C_2) - A'_2(K_1C_1 + K_2C_2)$, $P_2 = B'_2(K_1C_1 + K_2C_2) - (B_2/\gamma)(K_1C_1 - K_2C_2)$, $K_1 = (A_3 - iB_3 + \gamma(A'_3 - iB'_3))/2C_3$, and $K_2 = (A_3 - iB_3 - \gamma(A'_3 - iB'_3))/2C_4$.

The transmission probability, defined as $D(\varepsilon) = j_t/j_i$, is the transmitted probability current density relative to the incident probability current density, with probability current density $j = i\hbar/2m(\psi\nabla\psi^* - \psi^*\nabla\psi)$, which is obtained as

$$D(\varepsilon) = \frac{1}{\pi}\frac{1}{k_0}(2meF/\hbar^2)^{1/3}|T_t|^2. \quad (9)$$

The electron-emission current density can therefore be calculated by

$$J = e \int_0^\infty D(\varepsilon)N(\varepsilon)d\varepsilon, \quad (10)$$

where $D(\varepsilon)$ is given in Eq. (9) and $N(\varepsilon) = (mk_B T/2\pi^2\hbar^3)\ln[1 + \exp((E_F - \varepsilon)/k_B T)]$ is the flux of electrons with longitudinal energy ε impinging on the metal surface, k_B is the Boltzmann constant and T is the temperature [16, 57, 58]. For convenience, a short summary of the derivation of $N(\varepsilon)d\varepsilon$ is provided in the Supplemental Material [59].

III. RESULTS

A. Resonant tunneling through the quantum well

The quantum well formed due to ions, atoms, nanoparticles, etc. alters the surface-potential barrier, leading to strong resonant tunneling at certain energy levels [32, 60, 61], and thus, modulation of the field-emission current. Figure 2 shows a representative comparison of field emission from a bare metal surface and that with a nearby quantum well. The metal is gold, with a work function of $W = 5.1$ eV and Fermi energy of $E_F = 5.53$ eV. Unless stated otherwise, these are the default properties of the metal in this study. The energy diagram for a bare metal and metal surfaces with a quantum well ($d = 3$ nm, $L = 1.5$ nm, and $H = 6$ eV), under a dc field

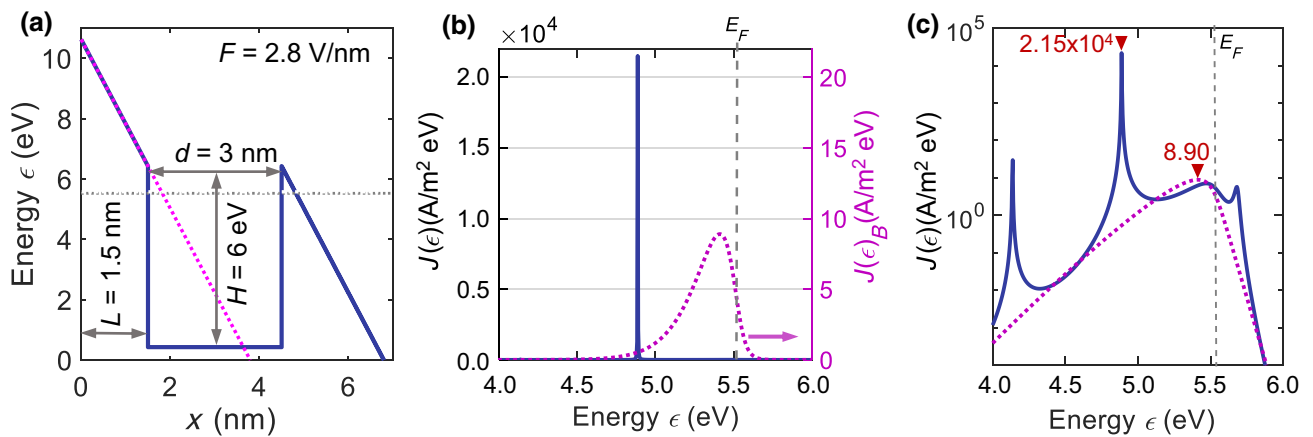


FIG. 2. (a) Energy diagram for a bare metal (magenta dashed line) and a metal surface with a quantum well of $d = 3$ nm, $L = 1.5$ nm, and $H = 6$ eV (blue solid line) under a dc field of $F = 2.8$ V/nm. (b) Emission-current-density energy spectrum for field emission without [calculated from Eq. (7) in Ref. [62]] and with a quantum well [calculated from Eq. (10)] as a function of initial electron energy ε ; (c) semilog plot of (b). We assume the metal is gold, with work function $W = 5.1$ eV and Fermi energy $E_F = 5.53$ eV. Temperature in Eq. (10) is taken as $T = 300$ K.

of $F = 2.8$ V/nm, is shown in Fig. 2(a). With the presence of a quantum well, electrons with initial energies between 0.43 and 6.43 eV have to tunnel through two separate barriers with the quantum well in between, which can produce resonant tunneling behavior. It can be found that the field-emission current density per energy, $J(\varepsilon) = eD(\varepsilon)N(\varepsilon)$, has a maximum resonance peak orders of magnitude higher than that for a bare metal surface, i.e., 2.15×10^4 A/m² eV versus 8.90 A/m² eV, as shown in Figs. 2(b) and 2(c). The corresponding total emission current densities are 105 and 3.07 A/m², respectively, showing a significantly enhanced emission current density with a quantum well. In the meantime, the energy spread of emitted electrons with a quantum well is orders of magnitude narrower than that from the bare metal surface, with a full width at half maximum (FWHM) of <0.008 eV versus about 0.3 eV in $J(\varepsilon)$, as shown in Figs. 2(b) and 2(c). This can be useful for producing collimated electron beams.

It has to be pointed out that the resonance is confined to a small region on nanostructures; there is image-charge-potential-induced modification of the well; coulomb wells are not square wells; and the well may be filled or depleted of charges with a time constant. In the case of field-emitter arrays, many tips contribute to the total emission current.

Because of these factors, the order of magnitude increase in 1D current density does not simply imply similar increases in total emitted current. Nevertheless, as shown in Fig. S1 within the Supplemental Material [59], the resonance effects inside the quantum well result in spikes on the current-field curves; this is similar to the experimental and theoretical observations of the current-voltage curves in Refs. [27,39,40].

Figures 3(a)–3(c) show the emission current density, calculated from Eq. (10), as a function of quantum well width d , under different dc fields F , well depths H , and distances to surface L , respectively. Multiple resonance peaks are clearly observed in these curves, some of which are indicated by downward triangles. As shown in Figs. 3(a) and 3(b), the increase of F and H results in the shift of the resonance peaks to smaller d . When L increases to 3 and 5 nm in Fig. 3(c), the curves show approximately periodic oscillations with more resonance peaks. The quantum well widths at which there are resonance peaks, obtained from $J-d$ curves in Figs 3(a)–3(c), are plotted as upward triangles connected with solid lines in Figs. 3(d)–3(f). Only the first five resonance peaks are shown in Figs. 3(d) and 3(e). In Fig. 3(f), when $L \geq 2.5$ nm, we show the position of every other resonance peak for the first ten peaks.

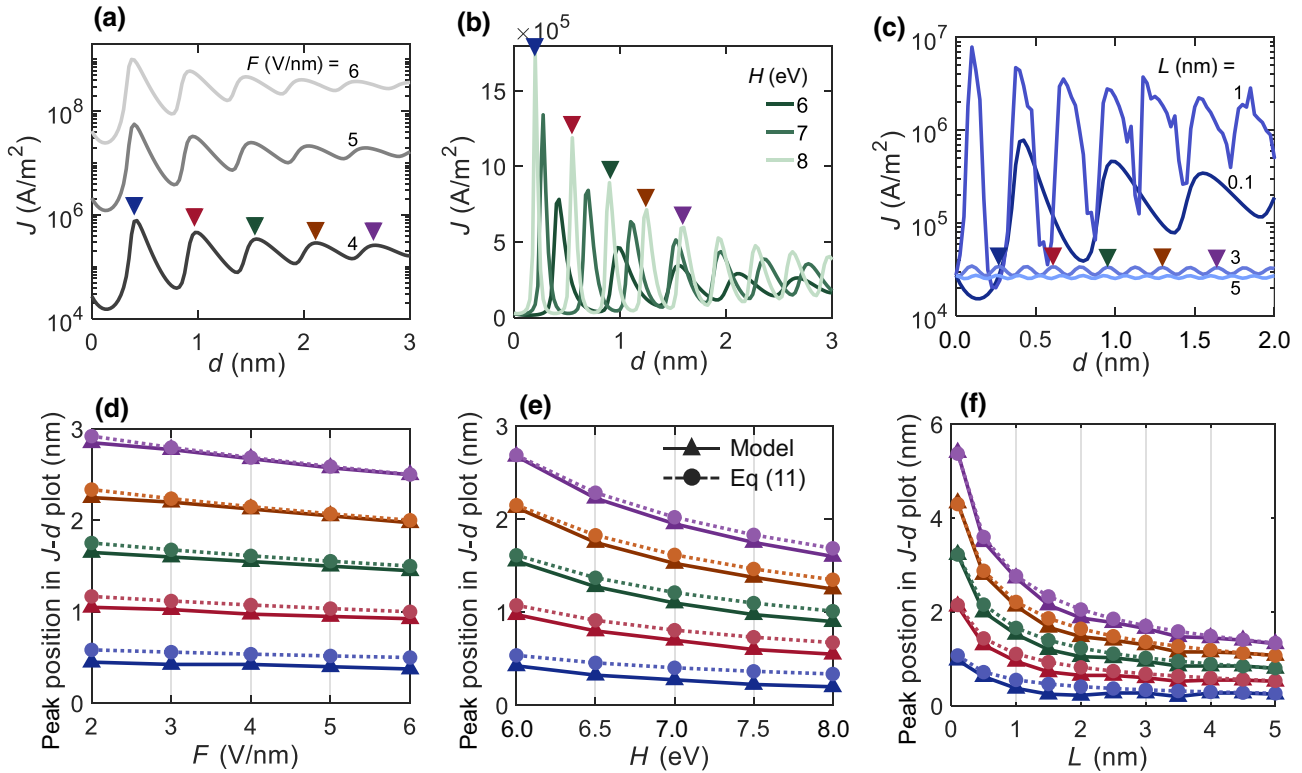


FIG. 3. Field-emission current density, calculated from Eq. (10), as a function of quantum well width d under different (a) dc field F , with $L = 0.1$ nm and $H = 6$ eV; (b) well depth H , with $L = 0.1$ nm and $F = 4$ V/nm; and (c) distance to surface L , with $H = 6$ eV and $F = 4$ V/nm. Quantum well width at which resonance peaks appear in $J-d$ plots at different (d) F , (e) H , and (f) L , corresponding to cases in (a)–(c), respectively. Upward triangles in (d)–(f) are extracted from Figs. 3(a)–3(c). Circles are calculated using Eq. (11). Temperature in Eq. (10) is taken as $T = 300$ K.

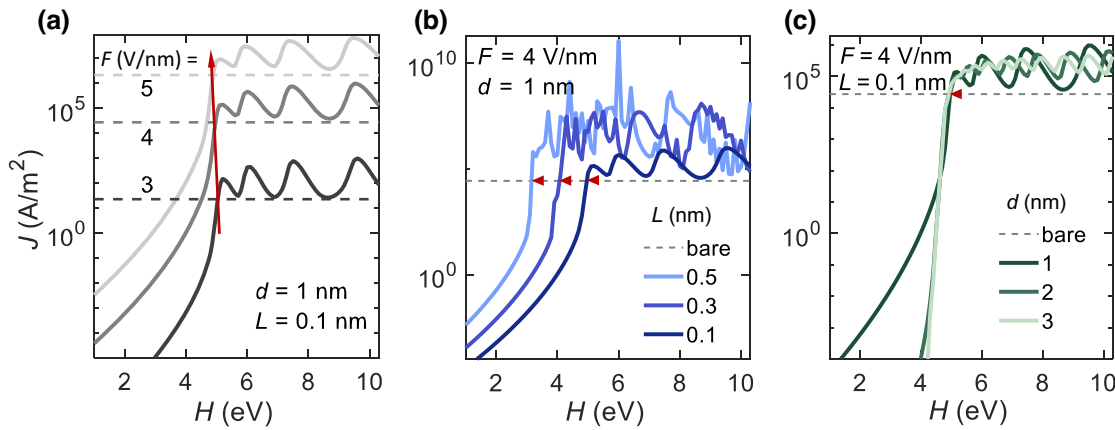


FIG. 4. Field-emission current density, calculated from Eq. (10), as a function of quantum well depth H under different (a) dc field F , with $d = 1 \text{ nm}$ and $L = 0.1 \text{ nm}$; (b) distance from the well to the metal surface L , with $d = 1 \text{ nm}$ and $F = 4 \text{ V/nm}$; and (c) quantum well width d , with $L = 0.1 \text{ nm}$ and $F = 4 \text{ V/nm}$. Temperature in Eq. (10) is taken as $T = 300 \text{ K}$. Horizontal dashed lines represent the emission current density from bare metal surfaces under the given dc field.

It is interesting to note that the relationship between well width and electron wavelength at which resonance peaks appear is given by

$$d = \frac{n\lambda}{2}, \quad n = 1, 2, 3, \dots . \quad (11)$$

Here, $\lambda = 2\pi/k$, with $k = \sqrt{2m[\varepsilon - (V_0 - H - eFL)]/\hbar^2}$ given in Eq. (5). Equation (11) also explains the variation of resonance peak position with F , H , and L . Since the majority of electron emission at room temperature occurs with the initial energy near E_F [53,63–65], we take $\varepsilon = E_F$ in Eq. (11), with other parameters being the same as those in Figs. 3(a)–3(c). The results are shown as circles connected with dashed lines in Figs. 3(d)–3(f). Good agreement between our exact model and Eq. (11) is obtained.

B. Enhanced field emission by the quantum well

Figure 4 shows the field-emission current density as a function of quantum well depth H under a different dc field F , distance from well to surface L , and quantum well width d . Horizontal dashed lines in each subfigure represent the emission current density from bare surfaces for a given dc electric field. It is found that the emission current density can be enhanced by the presence of quantum wells under certain conditions. The arrow in Fig. 4(a) and triangles in Figs. 4(b) and 4(c) indicate threshold H at which the emission current density from surfaces with a nearby quantum well equals that from bare surfaces. When F increases, this threshold H shifts towards a smaller value. As L increases from 0.1 to 0.5 nm with a constant interval of 0.2 nm, threshold H becomes smaller and the difference between those threshold values is almost equal. As

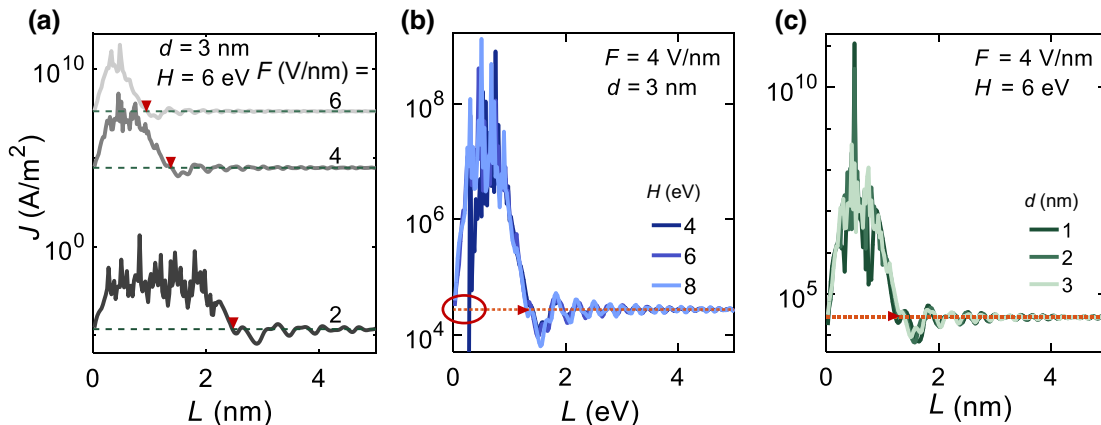


FIG. 5. Field-emission current density, calculated from Eq. (10), as a function of distance from the left edge of the well to the metal surface, L , under different (a) dc field F , with $d = 3 \text{ nm}$ and $H = 6 \text{ eV}$; (b) well depth H , with $d = 3 \text{ nm}$ and $F = 4 \text{ V/nm}$; and (c) well width d , with $H = 6 \text{ eV}$ and $F = 4 \text{ V/nm}$. Temperature in Eq. (10) is taken as $T = 300 \text{ K}$. Horizontal dashed lines represent the emission current density from bare surfaces under the given dc field.

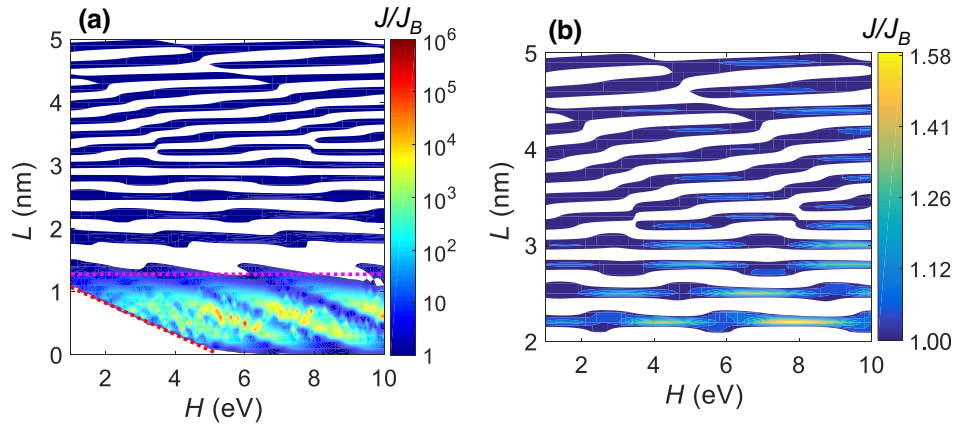


FIG. 6. (a) Normalized field-emission current J/J_B as a function of L and H , with J_B being the emission current density from bare metal surfaces; (b) detailed view of (a) for $L > 2$ nm. In (a), red dashed line corresponds to $eFL + H = W + 0.18$ eV, and horizontal magenta dashed line corresponds to $eFL = W$. Here, $F = 4$ V/nm and $d = 1$ nm.

shown in Fig. 4(c), under a different quantum well width d , threshold H remains unchanged. For those cases with H larger than the threshold value under given parameters, the presence of a quantum well shows an enhancement for the emission current density in general, and the current density oscillates with respect to H .

Figure 5 shows the field-emission current density as a function of distance from the left edge of the well to the surface, L , under different dc fields F , well depths H , and well widths d . These curves show two distinct regions: one with the emission current density enhanced by a few times to several orders of magnitude compared with the bare surface, and the other with the emission current density oscillating around the constant emission current density from bare surfaces. The separation of the two regions is indicated by red triangles. In the oscillation region, the oscillation magnitude is damped as L increases. The red ellipse in Fig. 5(b) indicates where the emission current

density starts to be enhanced compared to bare surfaces, which is similar to the points indicated by the arrows and triangles in Fig. 4.

It is of great interest to quantify the condition of the quantum well under which enhanced field emission occurs. According to the energy diagrams corresponding to Figs. 4 and 5 (see Figs. S2 and S3 within the Supplemental Material [59]), it is found that, when the quantum well satisfies

$$eFL + H \geq W + C, \quad (12)$$

with C being constant under the given dc field, the surface with a nearby quantum well starts to produce an enhanced field-emission current. In addition, the condition $eFL \approx W$ separates the strong enhancement region and the oscillation region, where the strong enhancement region is

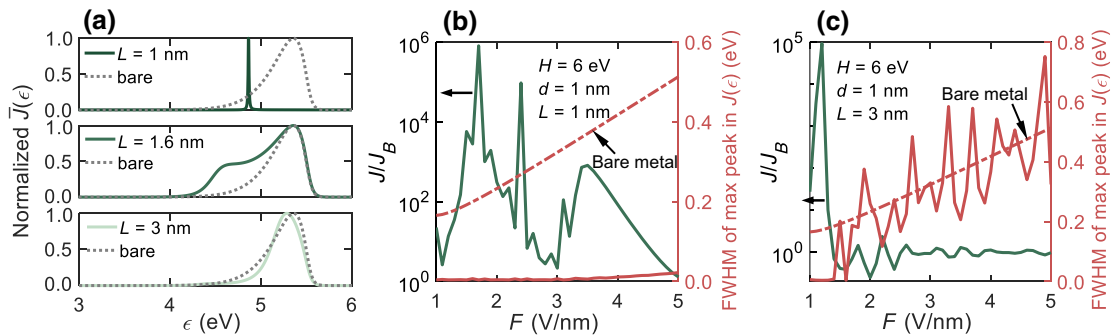


FIG. 7. Narrowing of the electron-emission-energy spectrum for enhanced field emission. (a) Normalized electron-emission-energy spectrum for surfaces with (green) and without (gray) a quantum well. From top to bottom, quantum well is with $L = 1$, 1.6 , and 3 nm, with fixed width $d = 1$ nm and depth $H = 6$ eV; dc field is $F = 4$ V/nm. (b),(c) Left axis, normalized field-emission current J/J_B , with J_B being the emission current density from bare metal surfaces (solid green line) as a function of F ; right axis, FWHM of the maximum peak in energy spectra as a function of F for surfaces without (dashed red line) and with a quantum well (solid red line). In (b), quantum well has $H = 6$ eV, $d = 1$ nm, and $L = 1$ nm. In (c), quantum well has $H = 6$ eV, $d = 1$ nm, and $L = 3$ nm.

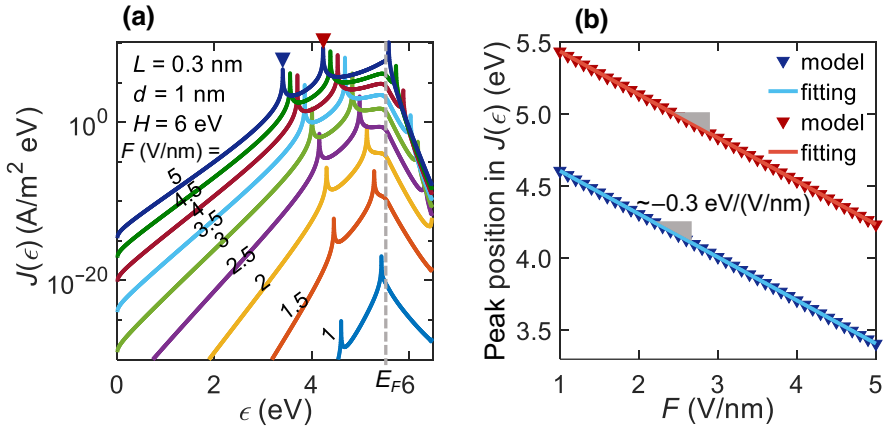


FIG. 8. (a) Field-emission energy spectrum, $J(\epsilon) = eD(\epsilon)N(\epsilon)$, under different dc fields F . Here, $L = 0.3$ nm, $d = 1$ nm, and $H = 6$ eV. Blue and red triangles indicate resonance peaks. (b) Resonance peak position in $J(\epsilon)$ as a function of dc field F .

bounded by

$$eFL \leq W. \quad (13)$$

Thus, L and H are two key properties that determine whether it can produce an enhanced field emission under a given dc field, through the two conditions in Eqs. (12) and (13).

Figure 6 plots the normalized emission current density, J/J_B , as a function of L and H , with J_B being the emission current density from bare surfaces, for $F = 4$ V/nm and $d = 1$ nm. The color regions show the enhancement part, i.e., $J/J_B > 1$, with an enhancement factor of up to 4.2×10^6 . The white region corresponds to emission suppression, i.e., $J/J_B < 1$. The red dashed line in Fig. 6(a) is $eFL + H = W + C$, with $C = 0.18$ eV, which overlaps with the lower-left boundary of the enhancement region. The horizontal magenta dashed line in Fig. 6(a) is $eFL = W$. The oscillation region, with alternating enhancement and suppression subregions, lies above this magenta dashed line. The enhancement subregion has an enhancement factor of no more than two, which is shown in Fig. 6(b). More calculations for normalized emission current density as a function of L and H under different combinations of d and F are given in Fig. S4 within the Supplemental Material [59]. The constant C shows no obvious dependence on d and increases when dc field strength F increases. Note that Jensen [40] modeled the resonance tunneling probability analytically as a Lorentzian with inputs derived from a transfer-matrix analysis [cf. Eq. (1) and Fig. 1 in this work with Eq. (22) and Fig. 3 of Ref. [40]]. A comparison of the current analysis of emission-current features under different L and H (e.g., in Fig. 6) using the Lorentzian approach would be useful; this requires further study.

C. Narrowing of the electron-emission-energy spectrum

Enhanced field emission due to quantum interference in the quantum well is characterized by narrowed resonance peaks in the electron-emission-energy spectrum. Figure 7(a) shows the normalized electron-emission current density per energy, $\bar{J}(\epsilon) = J(\epsilon)/J_{\max}(\epsilon)$, with respect to the maximum of $J_{\max}(\epsilon)$, with green solid (gray dashed) curves for field emission with (without) a quantum well. For $L = 1$, 1.6, and 3 nm, from top to bottom, the emission current density is 2.28×10^6 , 8.15×10^3 , and 3.06×10^4 A/m², respectively, compared to 2.73×10^4 A/m² for a bare metal surface. The greatly enhanced field emissions have higher peak values in the spectra, which are 1.29×10^8 , 1.13×10^4 , and 7.54×10^4 A/m² eV for $L = 1$, 1.6, and 3 nm, respectively, compared with 5.83×10^4 A/m² eV from a bare surface. The quantum well enhanced field emission also has a narrowed peak spectrum, which can be shown more clearly by the full width at half maximum (FWHM) of the maximum peak in the spectra in Figs. 7(b) and 7(c). The left axis in Figs. 7(b) and 7(c) shows the normalized field-emission current, J/J_B (with J_B being the emission current density from bare metal surfaces), as a function of F (green curves). It is obvious that $J/J_B > 1$ for the dc fields shown in Fig. 7(b), with the ratio ranging from 1.29 to 8.1×10^5 . The FWHM of the resonance peaks varies from 3.8×10^{-3} to 2.2×10^{-2} eV, which is significantly smaller than that of bare surfaces, as it varies from 0.17 to 0.51 eV, when F increases from 1 to 5 V/nm. In Fig. 7(c), enhanced field emission J/J_B is realized for $F < 1.4$ V/nm and the resonance peak width is also much narrowed. When $F > 1.4$ V/nm, J/J_B oscillates around 1, and the FWHM of the emission peak also oscillates around that of the bare surface. The observation that enhanced field emission is characterized by a narrowed spectrum is further confirmed by more calculations for different combinations of F , L , d ,

and H in Figs. S5 and S6 within the Supplemental Material [59].

D. Linear shift of resonance peaks with increasing dc field

Figure 8(a) shows the electron-emission current density per energy, $J(\varepsilon) = eD(\varepsilon)N(\varepsilon)$, under different dc fields, with $L = 0.3$ nm, $d = 1$ nm, and $H = 6$ eV. It is clear that the emission current density increases when the dc field increases. It is observed that resonance peaks shift towards smaller initial energy ε as F increases. The blue and red downward triangles indicate the first two resonance peaks from left to right on the spectrum. The initial energy where there is a resonance peak is shown as a function of dc field in Fig. 8(b). Downward triangles are obtained from the energy spectrum, with blue (red) ones corresponding to the first (second) resonance peak, as shown in Fig. 8(a). The position of the resonance peak in $J(\varepsilon)$ shows a linear relationship with F , with a fitting slope of approximately -0.3 eV/(V/nm). The fitting slope corresponds to $-eL$. The linear fitting curve is

$$\varepsilon_p = \varepsilon_{p0} - eFL. \quad (14)$$

Here, the y intercept is around the eigenenergy for electrons confined in a quantum well without a dc field, which can be obtained from Eq. (11) with $F = 0$ and is

$$\varepsilon_{p0} = E_F + W - H + \frac{\pi^2 \hbar^2}{2md^2} n^2, \quad n = 1, 2, 3, \dots. \quad (15)$$

The y intercept in Eq. (14) from linear fitting is 4.91 and 5.74 eV, respectively, for the first and second resonance peaks. Calculation of ε_{p0} from Eq. (15) gives 5.01 and 6.13 eV, respectively. Figure S7 within the Supplemental Material [59] provides more calculations for $L = 0.1$ and 3 nm. These results further confirm the linear relationship between the peak position in $J(\varepsilon)$ and dc field F in Eq. (14).

IV. CONCLUSION

We construct a quantum mechanical model for field emission from surfaces with nearby ions, atoms, nanoparticles, etc., which form a quantum well near the surfaces and modify the surface-potential barrier. The quantum well is simplified to be a square potential well with depth H , width d , and distance to the surface L . The exact analytical theory is developed by solving the 1D time-independent Schrödinger equation, which includes the effects of the metal surface (work function and Fermi energy) and quantum well (H , d , and L). It is found that the quantum well can lead to resonant enhanced field emission, with an enhancement factor greater than 10^5 compared to bare metal surfaces. The highly enhanced field emission is also characterized by significantly narrowed resonance peaks

(~50 times smaller) in the electron-emission-energy spectrum. The strong enhancement region is confined by the boundaries that $eFL + H > W + C$, with C being a constant dependent on F and $eFL \leq W$. It is also found that the resonance peaks in the electron-emission-energy spectrum shift linearly to smaller energy ε with increasing F , which follows $\varepsilon_p = \varepsilon_{p0} - eFL$, with ε_{p0} being approximately the eigenenergy for electrons confined in a potential well without a dc field. The theory provides insights for the design of high-efficiency emitters to produce highly collimated electron beams.

Quantum theory is valid for an arbitrary dc field (below the damage threshold). The fields in the dielectric region between the metal surface and the quantum well and in the vacuum are taken to be the externally applied dc field, without considering any field enhancement due to the geometrical effects and plasmonic effects [61,66] of the emitters and those of nearby ions, atoms, molecules, nanoparticles, etc. The 1D model may be applied to 3D nanostructures by considering the effective surface-field enhancement, in view of the promising outcome of similar treatments, as demonstrated by the good agreement of the 1D analytical quantum model for two-color laser-induced photoemission from nanotips, including field enhancement, with experimental results [67,68]; of the 1D analytical quantum model for pulsed-laser-induced photoemission with experiments of 3D laser spots [64,69]; and of applying a 1D tunneling model to study the time-dependent tunneling current in a THz-modulated STM nanotip [70]. The top and bottom edges of the well are assumed to remain horizontal without being distorted by a dc field or image charge field. A modification of the model with the field inside the well being considered (i.e., the bottom of the well with a slope of $-eF$) shows about 7.8% difference in the emission current density from the model in Fig. 1, when $L = 3$ nm, $d = 1$ nm, $H = 6$ eV, $F = 4$ V/nm, and the dc field inside the well is 2 V/nm. The field inside the quantum well will further lower the bottom of the well, which can shift the resonance peaks towards lower-electron-energy levels (results not shown, but can also be inferred from Fig. 8). It is also found that, when the dc field inside the quantum well decreases, the emission current density from the modified model gets closer to that calculated using the model in Fig. 1. The nonlinear surface field profile and more realistic surface potential with deformation may be considered. We have to resort to numerical methods, such as the transfer-matrix method.

While adopted here for simplicity and its exact analytical solution, the 1D quantum well approach is broadly used to study multilayered cathodes, nanoparticles on a metallic cathode surface, nanoprotrusion on top of a sharp emitter, etc.; these have shown good agreement with experiments [27,41,71]. Simple 1D models can give insights into important scaling of the physical properties and can capture the key features of resonant-tunneling-field-emission

current-voltage characteristics and energy distribution in 3D experiments. Our 1D model may even be directly used to capture the “irregular” shape of a realistic potential well, by approximating such a well with the corresponding square well to reserve the same resonances, as in Ref. [40] (see Fig. 4 therein). Nevertheless, it is shown that, when the ion is outside the metal, the model with a 3D ion potential results in a smaller tunneling probability than in the 1D potential model [72,73]. Detailed numerical calculations with 3D potential may be employed to provide quantitative evaluation when dealing with the cathode surface with nearby ions, atoms, and nanoparticles [73]. Such numerical calculations may be compared with the 1D model with effective surface field enhancement mentioned above.

It is also worthwhile to note that, while we consider a metal surface in this work, our theory is expected to be applicable to other materials as well, such as semiconductors or low-dimensional materials. The electron mass in all regions is currently assumed to be the electron rest mass, which may not be valid for multilayered semiconductor cathodes [16]. This can be done by changing the effective electron mass in the corresponding region. The density of states of semiconductors is different from that of metals, which has to be considered. As intuitively expected, an improvement in field-emission current density (e.g., Figs. 4 and 8) may indicate that the location of the bound states are being pulled into an energy region that the electron supply can access, thus resulting in emission peaks. Our analysis of how the location and properties of resonant structures impact emission may be used to examine the location and properties of such states. It may also be applied to qualitatively model tunneling during the motion of a charged ion towards the surface. There could be filling and depletion of charges in the well with a time constant; this can alter the potential profile [37]. It is shown that electron-confinement regions at the emitter surface (in the nanoparticles) have effects on the current-voltage relationship with steplike features [41]. A modification of the square quantum well of our model may be explored to consider the filling or depletion of charges in the well, by consistently solving Poisson’s equation together with the Schrödinger equation. The shot-noise-like emission behavior seen in semiconductor emitter cathodes [36] may also be implied from analysis using our model. A comparison of the energy distributions (e.g., shown in Fig. 7) to the energy-distribution measurements on silicon field emitters (e.g., Fig. 5 of Ref. [37]) invites speculation as to whether charged inclusions in the oxide are responsible for the energy-spectrum shifts under different gate voltages [38]. Further analysis using our model might help to reveal the role of charge inclusions in the well on the energy spectrum of emission, which are more relevant to materials such as semiconductors or low-dimensional materials. Future work may also include coupling this field-emission model with microscale gas breakdown, so we can have a

better understanding of the modified Paschen’s curve in a microscale gap. The work may further be extended to study photoemission [63,64,74] with quantum wells or in nanogaps [75,76], as well as secondary electron emission [77–79] with resonant structures.

ACKNOWLEDGMENTS

The MSU team is supported by the Office of Naval Research (ONR) YIP Grant No. N00014-20-1-2681, the Air Force Office of Scientific Research (AFOSR) Grant No. FA9550-20-1-0409, and the Air Force Office of Scientific Research (AFOSR) Grant No. FA9550-22-1-0523. The USC team is supported by the Office of Naval Research (ONR) YIP Grant No. N00014-21-1-2634, the Air Force Office of Scientific Research (AFOSR) Grant No. FA9550-22-1-0433, Air Force Office of Scientific Research (AFOSR) Grant No. FA9550-22-1-0430, Air Force Office of Scientific Research (AFOSR) Grant No. FA9550-21-1-0305, and Department of Energy (DOE) Grant No. DE-SC-0022248.

-
- [1] Q. H. Wang, A. A. Setlur, J. M. Lauerhaas, J. Y. Dai, E. W. Seelig, and R. P. H. Chang, A nanotube-based field-emission flat panel display, *Appl. Phys. Lett.* **72**, 2912 (1998).
 - [2] A. A. Talin, K. A. Dean, and J. E. Jaskie, Field emission displays: A critical review, *Solid-State Electron.* **45**, 963 (2001).
 - [3] Y. Saito, K. Hata, A. Takakura, J. Yotani, and S. Uemura, Field emission of carbon nanotubes and its application as electron sources of ultra-high luminance light-source devices, *Phys. B: Condens. Matter* **323**, 30 (2002).
 - [4] L. W. Swanson and G. A. Schwind, A review of field electron source use in electron microscopes, *Microsc. Microanal.* **11**, 864 (2005).
 - [5] F. Houdellier, L. de Knoop, C. Gatel, A. Masseboeuf, S. Mamishin, Y. Taniguchi, M. Delmas, M. Monthoux, M. J. Hÿtch, and E. Snoeck, Development of TEM and SEM high brightness electron guns using cold-field emission from a carbon nanotip, *Ultramicroscopy* **151**, 107 (2015).
 - [6] S. Sun, X. Sun, D. Bartles, E. Wozniak, J. Williams, P. Zhang, and C.-Y. Ruan, Direct imaging of plasma waves using ultrafast electron microscopy, *Struct. Dyn.* **7**, 064301 (2020).
 - [7] G. N. Fursey, Field emission in vacuum micro-electronics, *Appl. Surf. Sci.* **215**, 113 (2003).
 - [8] E. J. Radauscher, K. H. Gilchrist, S. T. Di Dona, Z. E. Russell, J. R. Piascik, J. J. Amsden, C. B. Parker, B. R. Stoner, and J. T. Glass, Improved performance of field emission vacuum microelectronic devices for integrated circuits, *IEEE Trans. Electron Devices* **63**, 3753 (2016).
 - [9] A. Evtukh, H. Hartnagel, O. Yilmazoglu, H. Mimura, and D. Pavlidis, *Vacuum Nanoelectronic Devices: Novel Electron Sources and Applications*, 1st ed. (Wiley, Chichester, West Sussex, United Kingdom, 2015).

- [10] J.-W. Han, D.-I. Moon, and M. Meyyappan, Nanoscale vacuum channel transistor, *Nano Lett.* **17**, 2146 (2017).
- [11] P. Zhang and Y. Y. Lau, Ultrafast and nanoscale diodes, *J. Plasma Phys.* **82**, 595820505 (2016).
- [12] P. Zhang, A. Valfells, L. K. Ang, J. W. Luginsland, and Y. Y. Lau, 100 years of the physics of diodes, *Appl. Phys. Rev.* **4**, 011304 (2017).
- [13] J. Lin, P. Y. Wong, P. Yang, Y. Y. Lau, W. Tang, and P. Zhang, Electric field distribution and current emission in a miniaturized geometrical diode, *J. Appl. Phys.* **121**, 244301 (2017).
- [14] G. Cao, Y. Z. Lee, R. Peng, Z. Liu, R. Rajaram, X. Calderon-Colon, L. An, P. Wang, T. Phan, S. Sultana, D. S. Lalush, J. P. Lu, and O. Zhou, A dynamic micro-CT scanner based on a carbon nanotube field emission x-ray source, *Phys. Med. Biol.* **54**, 2323 (2009).
- [15] D. H. Dowell, I. Bazarov, B. Dunham, K. Harkay, C. Hernandez-Garcia, R. Legg, H. Padmore, T. Rao, J. Smedley, and W. Wan, Cathode R&D for future light sources, *Nucl. Instrum. Methods Phys. Res., Sect. A* **622**, 685 (2010).
- [16] K. L. Jensen, *Introduction to the Physics of Electron Emission*, 1st ed. (Wiley, Hoboken, New Jersey, 2017).
- [17] N. A. Moody, K. L. Jensen, A. Shabaev, S. G. Lambrakos, J. Smedley, D. Finkenstadt, J. M. Pietryga, P. M. Anisimov, V. Pavlenko, E. R. Batista, J. W. Lewellen, F. Liu, G. Gupta, A. Mohite, H. Yamaguchi, M. A. Hoffbauer, and I. Robel, Perspectives on Designer Photocathodes for X-Ray Free-Electron Lasers: Influencing Emission Properties with Heterostructures and Nanoengineered Electronic States, *Phys. Rev. Appl.* **10**, 047002 (2018).
- [18] J. Smedley, T. Rao, and Q. Zhao, Photoemission studies on niobium for superconducting photoinjectors, *J. Appl. Phys.* **98**, 043111 (2005).
- [19] K. L. Jensen, Field emitter arrays for plasma and microwave source applications, *Phys. Plasmas* **6**, 2241 (1999).
- [20] D. Shiffler, T. K. Statum, T. W. Hussey, O. Zhou, and P. Mardahl, in *Modern Microwave and Millimeter Wave Power Electronics*, edited by R. J. Barker, N. C. Luhmann, J. H. Booske, and G. S. Nusinovich (IEEE, Piscataway, NJ, 2005), pp. 691.
- [21] D. Shiffler, M. Ruebush, M. LaCour, K. Golby, R. Umstattd, M. C. Clark, J. Luginsland, D. Zagar, and M. Sena, Emission uniformity and emission area of explosive field emission cathodes, *Appl. Phys. Lett.* **79**, 2871 (2001).
- [22] W. Tang, D. Shiffler, K. Golby, M. LaCour, and T. Knowles, Field enhancement for fiber emitters in linear and rectangular arrays, *J. Vac. Sci. Technol., B: Nanotechnol. Microelectron.: Mater., Process., Meas., Phenom.* **32**, 052202 (2014).
- [23] P. Zhang, S. B. Fairchild, T. C. Back, and Y. Luo, Field emission from carbon nanotube fibers in varying anode-cathode gap with the consideration of contact resistance, *AIP Adv.* **7**, 125203 (2017).
- [24] P. Zhang, J. Park, S. B. Fairchild, N. P. Lockwood, Y. Y. Lau, J. Ferguson, and T. Back, Temperature comparison of looped and vertical carbon nanotube fibers during field emission, *Appl. Sci.* **8**, 1175 (2018).
- [25] S. B. Fairchild, P. Zhang, J. Park, T. C. Back, D. Marincel, Z. Huang, and M. Pasquali, Carbon nanotube fiber field emission array cathodes, *IEEE Trans. Plasma Sci.* **47**, 2032 (2019).
- [26] P. Wong, P. Zhang, and J. Luginsland, Recent theory of traveling-wave tubes: A tutorial-review, *Plasma Res. Express* **2**, 023001 (2020).
- [27] V. Litovchenko, A. Evtukh, Yu. Kryuchenko, N. Goncharuk, O. Yilmazoglu, K. Mutamba, H. L. Hartnagel, and D. Pavlidis, Quantum-size resonance tunneling in the field emission phenomenon, *J. Appl. Phys.* **96**, 867 (2004).
- [28] R.-Z. Wang, W. Zhao, and H. Yan, Generalized mechanism of field emission from nanostructured semiconductor film cathodes, *Sci. Rep.* **7**, 43625 (2017).
- [29] M. Semenenko, S. Antonin, R. Redko, Y. Romanuyk, A. V. Hladkovska, V. Solntsev, and A. Evtukh, Resonant tunneling field emission of Si sponge-like structures, *J. Appl. Phys.* **128**, 114302 (2020).
- [30] J. D. Jarvis, H. L. Andrews, B. Ivanov, C. L. Stewart, N. de Jonge, E. C. Heeres, W.-P. Kang, Y.-M. Wong, J. L. Davidson, and C. A. Brau, Resonant tunneling and extreme brightness from diamond field emitters and carbon nanotubes, *J. Appl. Phys.* **108**, 094322 (2010).
- [31] Y. Li and D. B. Go, The quantum mechanics of ion-enhanced field emission and how it influences microscale gas breakdown, *J. Appl. Phys.* **116**, 103306 (2014).
- [32] X. Tan, P. Rumbach, N. Griggs, K. L. Jensen, and D. B. Go, Theoretical analysis of 1D resonant tunneling behavior in ion-enhanced cold field and thermo-field emission, *J. Appl. Phys.* **120**, 213301 (2016).
- [33] V. T. Binh, S. T. Purcell, N. Garcia, and J. Doglioni, Field-Emission Electron Spectroscopy of Single-Atom Tips, *Phys. Rev. Lett.* **69**, 2527 (1992).
- [34] S. T. Purcell, V. T. Binh, N. Garcia, M. E. Lin, R. P. Andres, and R. Reifenberger, Field emission from narrow bands above the Fermi level of nanometer-scale objects, *Phys. Rev. B* **49**, 17259 (1994).
- [35] M. E. Lin, R. P. Andres, and R. Reifenberger, Observation of the Discrete Electron Energy States of an Individual Nanometer-Size Supported Gold Cluster, *Phys. Rev. Lett.* **67**, 477 (1991).
- [36] D. Temple, W. D. Palmer, L. N. Yadon, J. E. Mancusi, D. Vellenga, and G. E. McGuire, Silicon field emitter cathodes: Fabrication, performance, and applications, *J. Vac. Sci. Technol., A* **16**, 1980 (1998).
- [37] J. Shaw, Effects of surface oxides on field emission from silicon, *J. Vac. Sci. Technol., B: Microelectron. Nanometer Struct. Process., Meas., Phenom.* **18**, 1817 (2000).
- [38] J. Shaw and J. Itoh, in *Vacuum Microelectronics*, edited by W. Zhu (John Wiley & Sons, New York, 2001), pp. 187.
- [39] V. G. Litovchenko, A. A. Evtukh, Yu. M. Litvin, N. M. Goncharuk, and V. E. Chayka, Observation of the resonance tunneling in field emission structures, *J. Vac. Sci. Technol., B: Microelectron. Nanometer Struct. Process., Meas., Phenom.* **17**, 655 (1999).
- [40] K. L. Jensen, On the application of quantum transport theory to electron sources, *Ultramicroscopy* **95**, 29 (2003).
- [41] L. D. Filip, M. Palumbo, J. D. Carey, and S. R. P. Silva, Two-step electron tunneling from confined electronic states in a nanoparticle, *Phys. Rev. B* **79**, 245429 (2009).

- [42] D. B. Go and A. Venkatraman, Microscale gas breakdown: Ion-enhanced field emission and the modified Paschen's curve, *J. Phys. D: Appl. Phys.* **47**, 503001 (2014).
- [43] G. Meng, X. Gao, A. M. Loveless, C. Dong, D. Zhang, K. Wang, B. Zhu, Y. Cheng, and A. L. Garner, Demonstration of field emission driven microscale gas breakdown for pulsed voltages using *in-situ* optical imaging, *Phys. Plasmas* **25**, 082116 (2018).
- [44] Y. Fu, P. Zhang, J. Krek, and J. P. Verboncoeur, Gas breakdown and its scaling law in microgaps with multiple concentric cathode protrusions, *Appl. Phys. Lett.* **114**, 014102 (2019).
- [45] A. L. Garner, G. Meng, Y. Fu, A. M. Loveless, R. S. Brayfield, and A. M. Darr, Transitions between electron emission and gas breakdown mechanisms across length and pressure scales, *J. Appl. Phys.* **128**, 210903 (2020).
- [46] A. L. Garner, A. M. Loveless, J. N. Dahal, and A. Venkatraman, A tutorial on theoretical and computational techniques for gas breakdown in microscale gaps, *IEEE Trans. Plasma Sci.* **48**, 808 (2020).
- [47] A. M. Loveless, L. I. Breen, and A. L. Garner, Analytic theory for field emission driven microscale gas breakdown for a pin-to-plate geometry, *J. Appl. Phys.* **129**, 103301 (2021).
- [48] W. S. Boyle and P. Kisliuk, Departure from Paschen's law of breakdown in gases, *Phys. Rev.* **97**, 255 (1955).
- [49] C. B. Duke and M. E. Alferieff, Field emission through atoms adsorbed on a metal surface, *J. Chem. Phys.* **46**, 923 (1967).
- [50] D. Penn, R. Gomer, and M. H. Cohen, Energy Distribution in Field Emission from Adsorbate-Covered Surfaces, *Phys. Rev. Lett.* **27**, 26 (1971).
- [51] Q. Huang, Instability of field emission from silicon covered with a thin oxide due to electron trapping, *J. Appl. Phys.* **79**, 3703 (1996).
- [52] P. D. Keathley, A. Sell, W. P. Putnam, S. Guerrera, L. Velásquez-García, and F. X. Kärtner, Strong-field photoemission from silicon field emitter arrays, *Ann. Phys. (Berlin)* **525**, 144 (2013).
- [53] Y. Zhou and P. Zhang, Theory of field emission from dielectric coated surfaces, *Phys. Rev. Res.* **2**, 043439 (2020).
- [54] K. F. Brennan and C. J. Summers, Theory of resonant tunneling in a variably spaced multiquantum well structure: An Airy function approach, *J. Appl. Phys.* **61**, 614 (1987).
- [55] K. L. Jensen, D. Finkenstadt, A. Shabaev, S. G. Lambrakos, N. A. Moody, J. J. Petillo, H. Yamaguchi, and F. Liu, A photoemission moments model using density functional and transfer matrix methods applied to coating layers on surfaces: Theory, *J. Appl. Phys.* **123**, 045301 (2018).
- [56] Y. Gohda and S. Watanabe, Theoretical analysis of field emission from atomically sharp aluminum tips, *Surf. Sci.* **516**, 265 (2002).
- [57] J. G. Simmons, Generalized formula for the electric tunnel effect between similar electrodes separated by a thin insulating film, *J. Appl. Phys.* **34**, 1793 (1963).
- [58] S. O. Kasap, *Electronic Materials and Devices* (McGraw-Hill, New York, 2006), pp. 336–339.
- [59] See the Supplemental Material <http://link.aps.org/supplemental/10.1103/PhysRevApplied.20.014043> for the supply function, $N(\varepsilon)$; effects of a dc field on field emission from surfaces with a nearby quantum well; energy diagram for field emission from surfaces with a nearby quantum well; boundaries separating the enhancement region and the oscillation region; narrowing of the electron-emission-energy spectrum; and the linear shift of resonance peaks in an energy spectrum with a dc field. It also contains Refs. [16,27,39,40,57,58].
- [60] C. Henkel, R. Zierold, A. Kommineni, S. Haugg, C. Thomasson, Z. Akksamija, and R. H. Blick, Resonant tunneling induced enhancement of electron field emission by ultra-thin coatings, *Sci. Rep.* **9**, 6840 (2019).
- [61] X. Xiong, Y. Zhou, Y. Luo, X. Li, M. Bosman, L. K. Ang, P. Zhang, and L. Wu, Plasmon-enhanced resonant photoemission using atomically thick dielectric coatings, *ACS Nano* **14**, 8806 (2020).
- [62] P. Zhang and T. Pan, Exact analytical theory for inverse tunneling of free vacuum electrons into a solid, *AIP Adv.* **7**, 065307 (2017).
- [63] Y. Zhou and P. Zhang, A quantum model for photoemission from metal surfaces and its comparison with the three-step model and Fowler–DuBridge model, *J. Appl. Phys.* **127**, 164903 (2020).
- [64] Y. Zhou and P. Zhang, Quantum efficiency of photoemission from biased metal surfaces with laser wavelengths from UV to NIR, *J. Appl. Phys.* **130**, 064902 (2021).
- [65] Y. Zhou and P. Zhang, Theory of laser-induced photoemission from a metal surface with nanoscale dielectric coating, *J. Appl. Phys.* **131**, 064903 (2022).
- [66] S. A. Maier, *Plasmonics: Fundamentals and Applications* (Springer, New York, U. S. A., 2007), Vol. 1.
- [67] Y. Luo and P. Zhang, Analysis of Two-Color Laser-Induced Electron Emission from a Biased Metal Surface Using an Exact Quantum Mechanical Solution, *Phys. Rev. Appl.* **12**, 044056 (2019).
- [68] M. Förster, T. Paschen, M. Krüger, C. Lemell, G. Wachter, F. Libisch, T. Madlener, J. Burgdörfer, and P. Hommelhoff, Two-Color Coherent Control of Femtosecond Above-Threshold Photoemission from a Tungsten Nanotip, *Phys. Rev. Lett.* **117**, 217601 (2016).
- [69] N. A. Papadogiannis, S. D. Moustaižis, and J. P. Girardeau-Montaut, Electron relaxation phenomena on a copper surface via nonlinear ultrashort single-photon photoelectric emission, *J. Phys. D: Appl. Phys.* **30**, 2389 (1997).
- [70] S. Banerjee and P. Zhang, Scaling of Time-Dependent Tunneling Current in Terahertz Scanning Tunneling Microscopes, *Phys. Rev. Appl.* **18**, 024011 (2022).
- [71] C. W. Johnson, A. K. Schmid, M. Mankos, R. Röpke, N. Kerker, I. S. Hwang, E. K. Wong, D. F. Ogletree, A. M. Minor, and A. Stibor, Electron-Beam Source with a Superconducting Niobium Tip, *Phys. Rev. Appl.* **19**, 034036 (2023).
- [72] N. Lorente, R. Monreal, and M. Alducin, Local theory of Auger neutralization for slow and compact ions interacting with metal surfaces, *Phys. Rev. A* **49**, 4716 (1994).
- [73] M. A. Cazalilla, N. Lorente, R. D. Muñoz, J.-P. Gauyacq, D. Teillet-Billy, and P. M. Echenique, Theory of Auger neutralization and deexcitation of slow ions at metal surfaces, *Phys. Rev. B* **58**, 13991 (1998).

- [74] Y. Luo, Y. Zhou, and P. Zhang, Few-cycle optical-field induced photoemission from biased surfaces: An exact quantum theory, *Phys. Rev. B* **103**, 085410 (2021).
- [75] Y. Luo and P. Zhang, Ultrafast optical-field-induced photo-electron emission in a vacuum nanoscale gap: An exact analytical formulation, *Appl. Phys. Lett.* **119**, 194101 (2021).
- [76] Y. Luo and P. Zhang, Optical-Field-Induced Electron Emission in a dc-Biased Nanogap, *Phys. Rev. Appl.* **17**, 044008 (2022).
- [77] A. Iqbal, J. Ludwick, S. Fairchild, M. Cahay, D. Gortat, M. Sparkes, W. O'Neill, T. C. Back, and P. Zhang, Empirical modeling and Monte Carlo simulation of secondary electron yield reduction of laser drilled microporous gold surfaces, *J. Vac. Sci. Technol., B* **38**, 013801 (2019).
- [78] J. Ludwick, A. Iqbal, D. Gortat, J. D. Cook, M. Cahay, P. Zhang, T. C. Back, S. Fairchild, M. Sparkes, and W. O'Neill, Angular dependence of secondary electron yield from microporous gold surfaces, *J. Vac. Sci. Technol., B* **38**, 054001 (2020).
- [79] M. Mirmozafari, A. Iqbal, P. Zhang, N. Behdad, J. H. Booske, and J. P. Verboncoeur, Secondary electron yield characterization of high porosity surfaces for multipactor-free microwave components, *Phys. Plasmas* **29**, 082109 (2022).

Theoretical Analysis of Resonant Tunneling Enhanced Field Emission

Yang Zhou¹, Ragib Ahsan², and Hyun Uk Chae², Rehan Kapadia², and Peng Zhang^{1,*}

¹Department of Electrical and Computer Engineering, Michigan State University, East Lansing, Michigan 48824, USA

²Ming Hsieh Department of Electrical and Computer Engineering, University of Southern California, Los Angeles, California 90089, USA

*Corresponding to: pz@egr.msu.edu

Supplementary material

1. Supply function $N(\varepsilon)$

The following derivation is based on refs [1-3].

$N(\varepsilon)d\varepsilon$ gives the flux of electrons with initial longitudinal energy (energy component in x direction) between ε and $\varepsilon+d\varepsilon$ impinging on the metal surface, which is obtained by integrating the product of metal's three-dimensional (3D) electron density of state (DOS) with probability of occupation of the states over the transverse momentum (or velocity) components,

$$N(k_x)dk_x = \int_{-\infty}^{\infty} dk_y \int_{-\infty}^{\infty} dk_z \left(\frac{1}{\pi^3} \frac{2}{8} \right) f(E) v_x dk_x \quad (S1)$$

where $2/(8\pi^3)$ is the number of states per unit volume in momentum space (k -space), with 2 accounting for the two states of electrons of opposite spins for a given \vec{k} state and $1/8$ accounting for the indistinguishable quantum state differed only in sign in the three dimensions, $f(E) = 1/\left[1 + \exp\left(\frac{E-E_F}{k_B T}\right)\right]$ is the Fermi-Dirac distribution, and $v_x = \sqrt{2E_x/m}$ the velocity along x direction. Transform the integral from cartesian coordinate to polar coordinate, we obtain

$$N(k_x)dk_x = \int_0^{2\pi} d\theta \int_0^{\infty} k_r dk_r \left(\frac{1}{4\pi^3} \right) f(E) v_x dk_x \quad (S2)$$

From $E - E_c = \frac{\hbar^2 k^2}{2m}$ with the bottom of conduction band $E_c = 0$ in our model (see Fig. 1), $dk =$

$\frac{m}{\hbar\sqrt{2mE}} dE$, and therefore $k_r = \frac{\sqrt{2mE_r}}{\hbar}$, $dk_r = \frac{m}{\hbar\sqrt{2mE_r}} dE_r$, $dk_x = \frac{m}{\hbar\sqrt{2mE_x}} dE_x$, $E = E_x + E_r$. Thus,

Eq. (S2) can be written as

$$\begin{aligned}
N(E_x)dE_x &= 2\pi \int_0^\infty \frac{m}{\hbar^2} dE_r \left(\frac{1}{4\pi^3} \right) \frac{1}{1 + \exp \left(\frac{E_r + E_x - E_F}{k_B T} \right)} \sqrt{\frac{2E_x}{m}} \frac{m}{\hbar \sqrt{2mE_x}} dE_x \\
&= \frac{m}{2\pi^2 \hbar^3} dE_x \int_0^\infty \frac{1}{1 + \exp \left(\frac{E_r + E_x - E_F}{k_B T} \right)} dE_r = \frac{mk_B T}{2\pi^2 \hbar^3} \ln \left(1 + e^{\frac{E_F - E_x}{k_B T}} \right) dE_x
\end{aligned} \tag{S3}$$

Since $\varepsilon = E_x$, Eq. (S3) becomes $N(\varepsilon)d\varepsilon$ in Eq. (10), in the unit of $\frac{1}{m^2 \cdot s}$.

2. Effects of dc field on field emission from surfaces with a nearby quantum well

Figure S1 shows the electron emission current as a function of applied dc field. Spikes can be observed at certain fields, and they shift when the quantum properties (d , L , and H) change. Resonance effects induced spikes are similar to the experimental and theoretical observations on the current-voltage curves in Ref. [4-6].

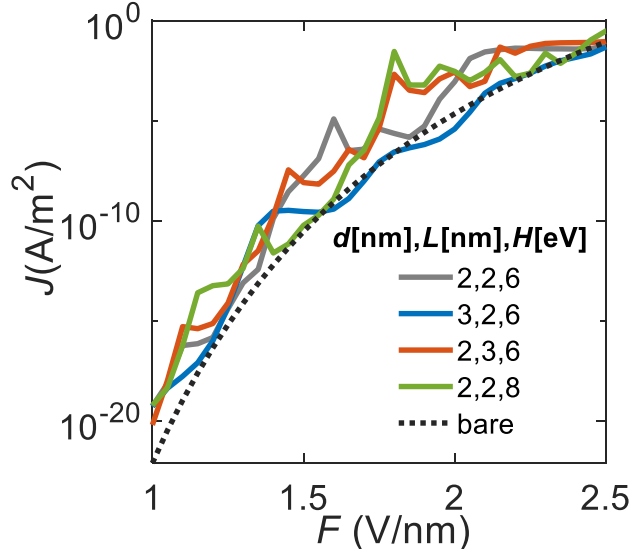


Figure S1. Electron emission current as a function of applied dc electric field under various quantum well properties.

3. Energy diagram for field emission from surfaces with a nearby quantum well

Figure S2 shows energy diagrams for cases indicated by arrowed curve and triangles in Fig. 4 in the main text. The arrowed curve and triangles indicate the threshold H value at which the

emission current from metal surfaces with a nearby quantum well equals that from bare metal surfaces. These threshold H values are shown for each curve in Fig. S2. It can be found that the bottom of the quantum well is just below the Fermi level, i.e., $eFL + H = W + C$ with C being constant dependent on F (see Fig. S4).

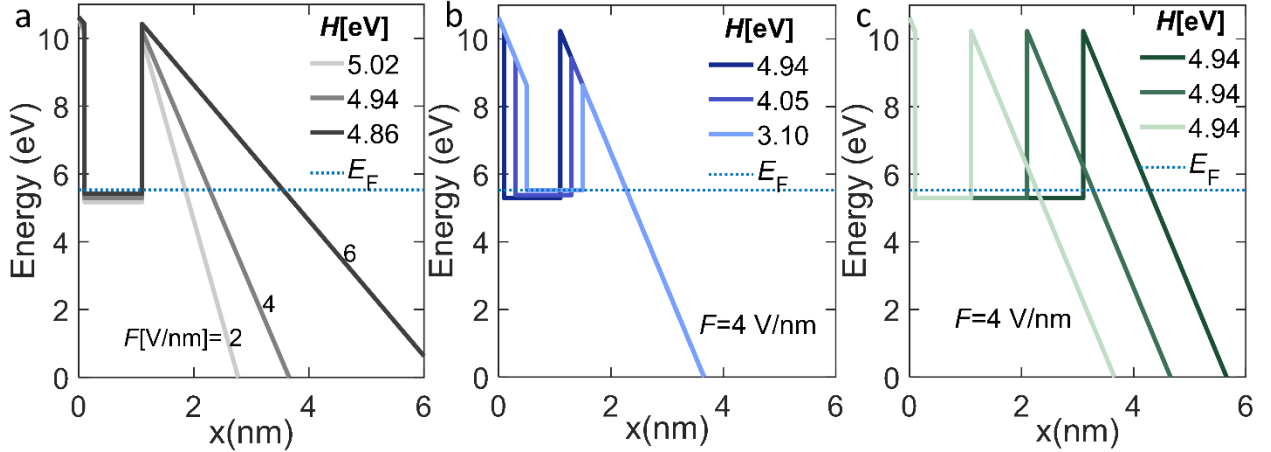


Figure S2. Energy diagram for field emission from metal surfaces with a nearby quantum well with threshold well depth H under a different (a) dc field F ; (b) distance between the quantum well and the surface L ; (c) well width d . In (a), $L = 0.1$ nm, and $d = 1$ nm. In (b), $F = 4$ V/nm, and $d = 1$ nm. In (c), $F = 4$ V/nm, and $L = 0.1$ nm.

Figure S3 shows energy diagrams for cases indicated by triangles in Fig. 5(a) in the main text. The triangles indicate the L value at which the emission current from metal surfaces with a nearby quantum well as a function of L is separated into two regions, i.e., the enhancement region and the oscillation region. It can be observed from Fig. S3 that around these L values the top of the quantum well falls closely above or below the Fermi level, i.e., $eFL \approx W$.

Therefore, the conditions of $eFL + H = W + C$ and $eFL \approx W$ bound the region where there is strongly enhanced field emission current, and $eFL > W$ refers to the oscillation region where there is alternating enhanced and suppressed field emission compared to bare surfaces.

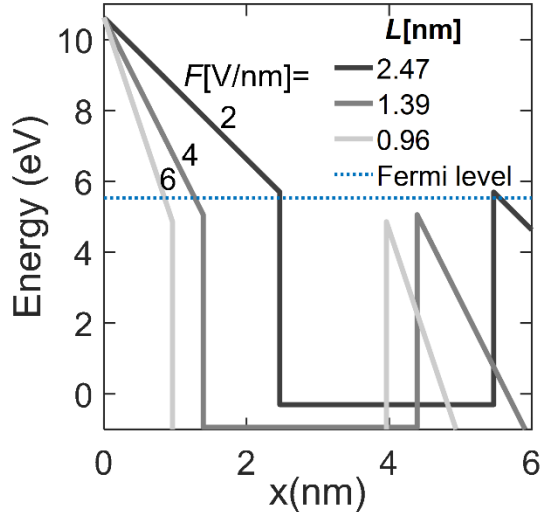


Figure S3. Energy diagram for field emission from metal surfaces with a nearby quantum well with different distances to the surface L under different dc fields F . Here, $d = 3$ nm and $H = 6$ eV.

4. Boundaries separating the enhancement region and the oscillation region

Figure S4 presents normalized emission current density J/J_B as a function of L and H under different combinations of d and F , with J_B being the emission current density from bare surfaces. The white region corresponds to the suppression region which has an emission current smaller than that from bare surfaces. The color region corresponds to the enhancement region. The area enclosed by the red dashed line and magenta dashed line confines the strong enhancement region with an enhancement factor much larger than 1. The red line is $eFL + H = W + C$. When F increases from 4 V/nm (Fig. 6 in the main text) to 6 V/nm (Fig. S4(a)) and 8 V/nm (Fig. S4(b)), the constant C increases from 0.18 eV to 0.3 eV and 0.5 eV. C shows its dependence on dc field F . When d increases from 1 nm (Fig. 6 in the main text) to 2 nm (Fig. S4(c)) and 3 nm (Fig. S4(d)), the constant C remains unchanged as 0.18 eV.

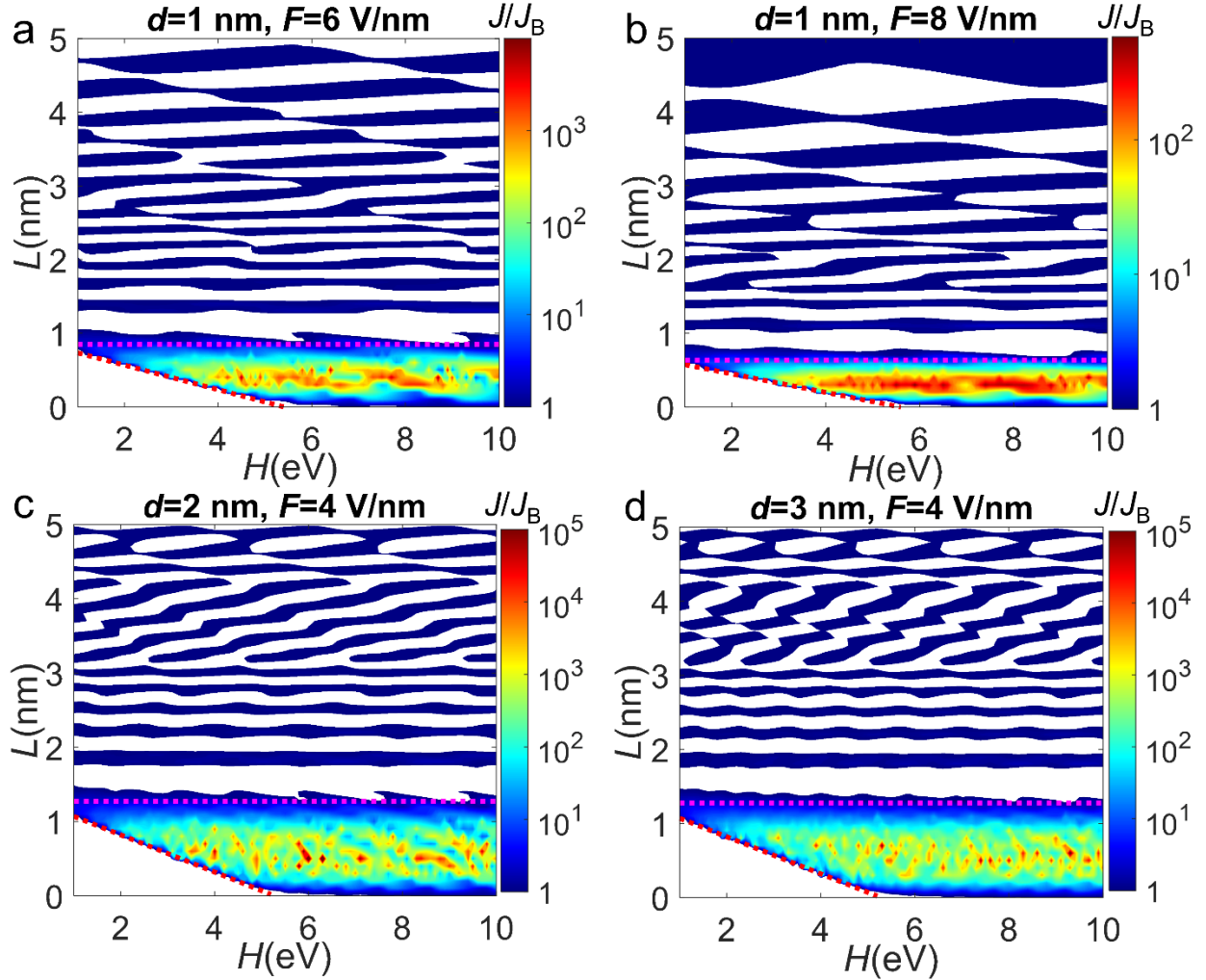


Figure S4. Normalized field emission current J/J_B as a function of L and H under different combinations of d and F . (a) $d = 1$ nm and $F = 6$ V/nm; (b) $d = 1$ nm and $F = 8$ V/nm; (c) $d = 2$ nm and $F = 4$ V/nm; (d) $d = 3$ nm and $F = 4$ V/nm. J_B is the emission current density from bare metal surfaces. The red dashed lines corresponds to (a) $eFL + H = W + 0.3$ eV; (b) $eFL + H = W + 0.5$ eV; (c) $eFL + H = W + 0.18$ eV; (d) $eFL + H = W + 0.18$ eV. The magenta dashed line corresponds to $eFL = W$.

5. Narrowing of electron emission energy spectrum

Figure S5 shows the ratio of the emission current density J to that from bare surfaces J_B (left axis) and the FWHM of the maximum resonance peak in electron emission energy spectra (right axis) as a function of F for $L = 0.5$ nm and $L = 1.6$ nm with $H = 6$ eV and $d = 1$ nm. It can be observed from Fig. S5(a) that the emission current density enhancement factor is ≥ 2.47 and

FWHM is $\sim 4 \times 10^{-3}$ eV compared to > 0.17 eV for bare surface. As shown in Fig. S5(b), the strong enhancement regions, $1 \leq F \leq 1.5$ V/nm, and $1.9 \leq F \leq 2.8$ V/nm, with enhancement factor > 2 , have their FWHM ~ 70 times smaller than that of the bare surfaces. When $J/J_B \approx 1$, its FWHM also oscillates around that of bare surfaces.

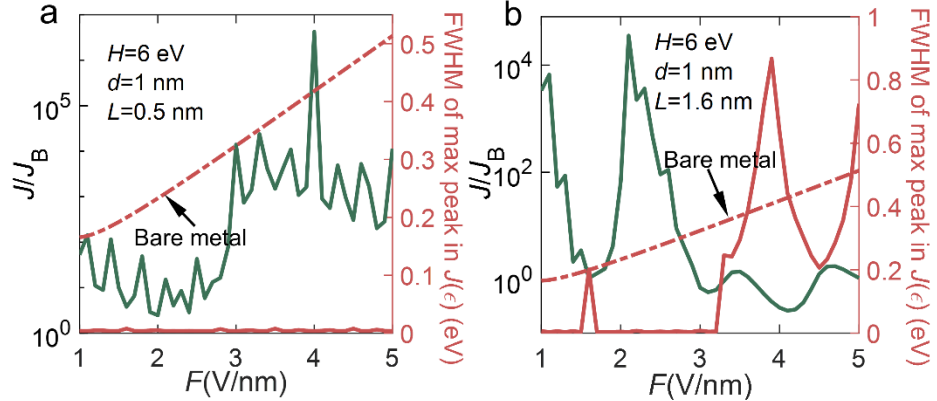


Figure S5. Left axis: J/J_B (green) as a function of F ; Right axis: Full width half maximum (FWHM) of the maximum peak in energy spectra as a function of F . In (a), the quantum well has $H = 6$ eV, $d = 1$ nm, and $L = 0.5$ nm. In (b), the quantum well has $H = 6$ eV, $d = 1$ nm, and $L = 1.6$ nm.

Figure S6 shows J/J_B (left axis) and FWHM of the emission peak in electron emission energy spectra (right axis) as a function of L (Fig. S6(a) and S6(b)), H (Fig. S6(c) and S6(d)), and d (Fig. S6(e) and S6(f)). It further confirms that the strong enhancement region is also characterized by a narrowed resonance peak and that $J/J_B \sim 1$ is characterized by a peak width close to that of bare surfaces.

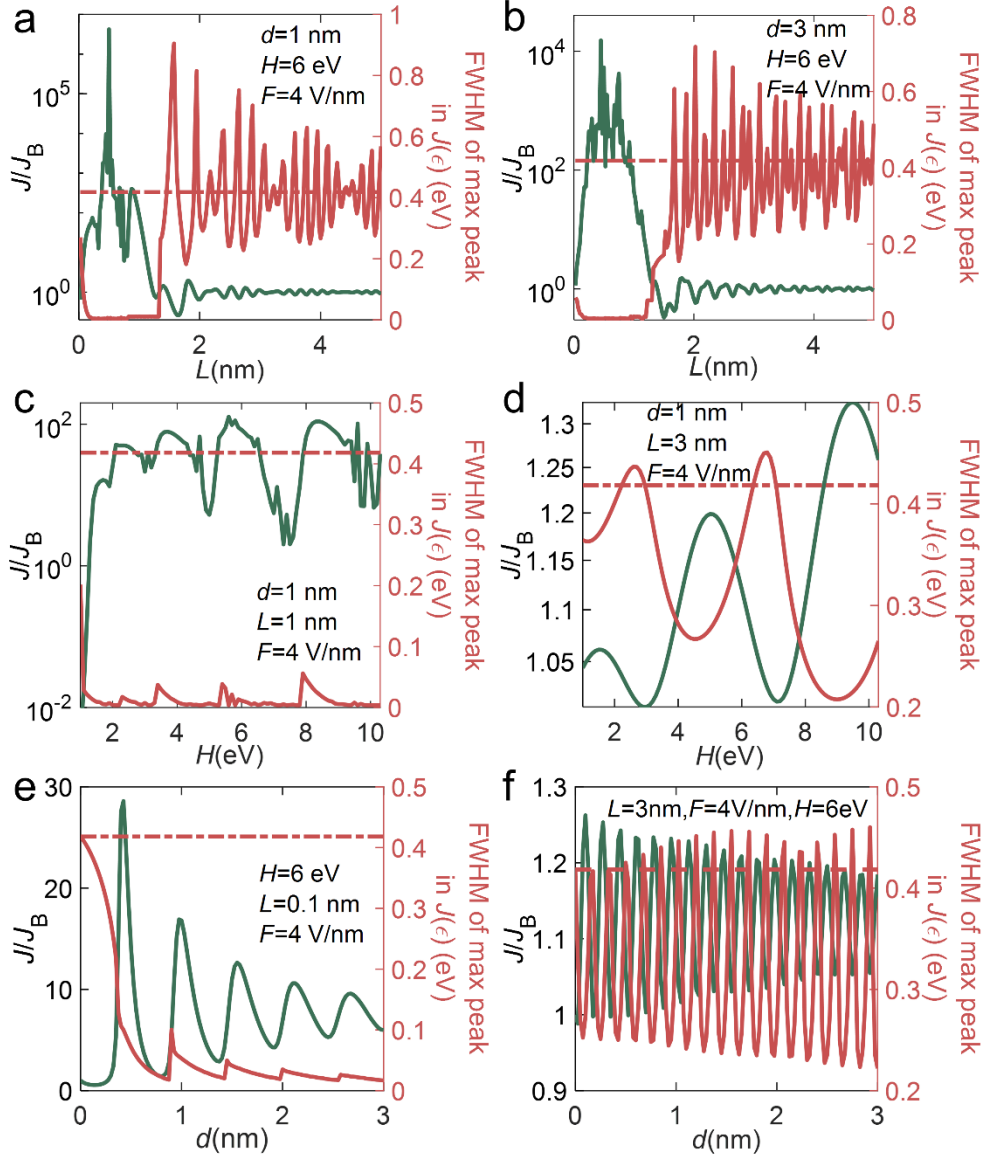


Figure S6. J/J_B (green) and FWHM of the maximum peak in energy spectra (red) as a function of (a) and (b) L ; (c) and (d) H ; and (e) and (f) d , for surfaces without (dashed red line) and with (solid red line) a quantum well.

6. Linear shift of resonance peaks in energy spectrum with dc field

Figures S7(a) and S7(b) show electron emission current density per energy, $J(\varepsilon) = eD(\varepsilon)N(\varepsilon)$, under different dc fields, for $L = 0.1$ nm and $L = 3$ nm, respectively. The triangles in Fig. S7(a) and arrowed lines in Fig. S7(b) indicate resonance peaks on the electron emission energy spectra, and their corresponding positions are extracted and plotted as triangles in Figs. S7(c) and

S7(d) respectively. The linear fittings, shown as solid lines in Figs. S7(c) and S7(d), result in slopes of $\sim -0.1 \text{ eV}/(\text{V/nm})$ and $\sim -3 \text{ eV}/(\text{V/nm})$, respectively, which are $\sim -eL$, as in Eq. (14) in the main text. The fitted y -intercepts in Fig. S7(c) are 4.91 eV and 5.73 eV, which are close to the eigenenergies of 5.01 eV and 6.13 eV calculated from Eq. (15) in the main text. The fitted y -intercepts in Fig. S7(d) are 4.91 eV, 5.74 eV, and 7.09 eV, which are close to the eigenenergies of 5.01 eV, 6.13 eV, and 8.01 eV calculated from Eq. (15) in the main text. It is found that lower eigenenergies match better with those fitted y -intercepts.

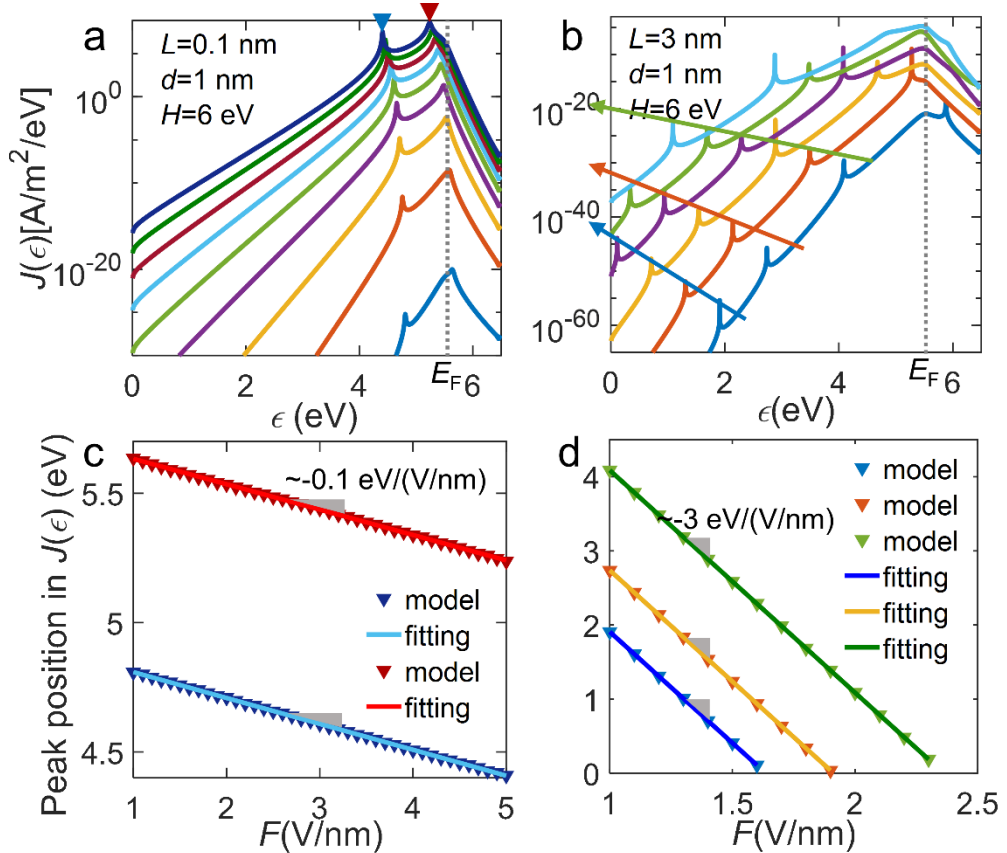


Figure S7. (a) and (c) Field emission energy spectrum, calculated from $J(\epsilon) = eD(\epsilon)N(\epsilon)$, under different dc fields F . In (a) $L = 0.1 \text{ nm}$, $d = 1 \text{ nm}$, and $H = 6 \text{ eV}$ and in (b) $L = 3 \text{ nm}$, $d = 1 \text{ nm}$, and $H = 6 \text{ eV}$. (b) and (d) Resonance peak position in $J(\epsilon)$ as a function of dc field F .

References

- [1] J. G. Simmons, *Generalized formula for the electric tunnel effect between similar electrodes separated by a thin insulating film*, Journal of applied physics **34**, 1793 (1963).
- [2] K. L. Jensen, *Introduction to the Physics of Electron Emission*, 1 edition (Wiley, Hoboken, New Jersey, 2017), p. 127-128.
- [3] S. O. Kasap, *Electronic materials and Devices*, McGraw-Hill New York (2006), p. 336-339.
- [4] V. Litovchenko, A. Evtukh, Y. Kryuchenko, N. Goncharuk, O. Yilmazoglu, K. Mutamba, H. L. Hartnagel, D. Pavlidis, *Quantum-size resonance tunneling in the field emission phenomenon*, Journal of applied physics **96**, 867 (2004).
- [5] V.G. Litovchenko, A.A. Evtukh, Y.M. Litvin, N.M. Goncharuk, and V.E. Chayka, *Observation of the resonance tunneling in field emission structures*, Journal of Vacuum Science & Technology B: Microelectronics and Nanometer Structures Processing, Measurement, and Phenomena **17**, 655 (1999).
- [6] K.L. Jensen, *On the application of quantum transport theory to electron sources*, Ultramicroscopy **95**, 29 (2003).